Journal of
Materials Chemistry C

ROYAL SOCIETY OF CHEMISTRY

PAPER

View Article Online
View Journal | View Issue

Check for updates

Cite this: *J. Mater. Chem. C*, 2025, **13**, 17056

Experimental and theoretical insights into light confinement within 2D waveguides of alkylphenyl benzothiadiazole crystals†

Iván Torres-Moya,[a] Mohammad Afsar Uddin,[b] Sergio Gámez-Valenzuela,[cg] Javier Álvarez-Conde,[d] Juan Cabanillas-González,[d] Ana L. Montero-Alejo,[e] Ana M. Rodriguez,[a] Luis A. Montero-Cabrera,[fh] M. Carmen Ruiz Delgado,*[cg] Berta Gómez-Lor*[b] and Pilar Prieto*[a]

Received 14th May 2025,
Accepted 18th July 2025

DOI: 10.1039/d5tc01924a

rsc.li/materials-c

In this work, an experimental and theoretical investigation was carried out to explore the key factors influencing light transmission mechanisms in organic crystalline materials. Three benzothiadiazole (BTD) derivatives with slight structural modifications were selected due to their strong self-assembly capabilities, which enabled control over molecular packing and waveguide behavior. High-quality single crystals were obtained *via* the slow diffusion method, revealing distinct waveguiding properties: **B1** and **B2** function as two-dimensional (2D) waveguides, whereas **B3** behaves as a one-dimensional (1D) waveguide. These differences arise from variations in crystal packing and directional S–N interactions, which consistently guide growth along the [100] direction. In **B3**, the dominance of S–N interactions solely along this axis promotes fiber formation, while **B1** and **B2** benefit from a more favorable dipole-field alignment in both longitudinal and transverse directions. Optical loss coefficients (OLC) indicate that **B1** and **B2** perform better as optical waveguides, exhibiting significantly lower losses ($2–8.7 \times 10^{-3}$ dB μm^{-1}) compared to **B3** (1.07×10^{-2} dB μm^{-1}). These differences are attributed to variations in exciton energy, as determined by the CIS|CNDOL/1CS method applied to simulated aggregates for both molecules and crystals, which imply more localized Frenkel excitons with a greater ability to generate polaritons and, therefore, a better capability to transmit light. They are also attributed to disparities in microchannel size and density within the crystal structures. The insights gained provide a comprehensive understanding of the key factors that influence light transmission.

Introduction

The development and implementation of physical structures known as optical waveguides, capable of confining and efficiently guiding light, have driven major advancements in the fields of communication, leading to faster data transfer, and improved medical treatments. The groundbreaking discovery by Charles K. Kao that information could be transmitted *via* light fundamentally transformed global communication through optical fiber networks,[1–5] significantly enhancing connectivity, transmission speed, high-definition capabilities, and bandwidth capacity.

However, while significant progress has been made at the macroscopic scale, the development of efficient optical waveguides at the microscopic level remains a formidable challenge, requiring further research and technological innovation.

In recent decades, substantial research efforts have been dedicated to the development of nano- and microscale waveguides fabricated from organic materials,[6–9] which constitute

---

[a] *Department of Inorganic, Organic Chemistry and Biochemistry, Faculty of Chemical Science and Technologies, University of Castilla-La Mancha (UCLM)-IRICA, 13071 Ciudad Real, Spain. E-mail: MariaPilar.Prieto@uclm.es*
[b] *Institute of Materials Science of Madrid (ICMM-CSIC), Sor Juana Inés de la Cruz 3, Cantoblanco, 28049 Madrid, Spain. E-mail: bgl@icmm.csic.es*
[c] *Department of Physical Chemistry, University of Málaga, Campus de Teatinos s/n, 29071 Málaga, Spain. E-mail: carmenrd@uma.es*
[d] *Madrid Institute for Advanced Studies, IMDEA Nanociencia, Calle Faraday 9, Ciudad Universitaria de Cantoblanco, 28049 Madrid, Spain*
[e] *Departamento de física, Facultad de Ciencias Naturales, Matemática y del Medio Ambiente (FCNMM), Universidad Tecnológica Metropolitana, Ñuñoa, 7800002 Santiago, Chile*
[f] *Computational and Theoretical Chemistry Laboratory, Department of Physical Chemistry, Faculty of Chemistry, University of Havana, 10400 Havana, Cuba*
[g] *Instituto Universitario de Materiales y Nanotecnología, IMANA, University of Málaga, Campus de Teatinos, 29071, Málaga, Spain*
[h] *Donostia International Physics Center (DIPC), 20018 Donostia – San Sebastián, Basque, Spain*

† Electronic supplementary information (ESI) available. CCDC 2450828 (**B2**), 2450829 (**B1**) and 2074632 (**B3**). For ESI and crystallographic data in CIF or other electronic format see DOI: https://doi.org/10.1039/d5tc01924a

exceptional candidates for crystal engineering and often exhibit superior properties compared to their inorganic counterparts. They possess unique traits, such as the ability to self-assemble into highly crystalline structures with minimal defects, diverse morphologies, excellent thermal stability, straightforward solution-processability and high photoluminescence (PL) efficiency. A particularly notable feature of these materials is their tunability: their optical properties can be precisely tailored by modifying the molecular structure, tuning the packing arrangement or applying strategic doping methods which directly influence their photophysical behavior.[10]

Recently, innovative waveguides based on organic materials have been reported, showcasing unique properties that enable advanced functionalities for practical device applications. Among these features are chirality,[11] anisotropy,[12] mechanical flexibility,[13] responsiveness to external stimuli[14–16] and phosphorescence behaviour.[17] Understanding how light propagates through crystal structures and predicting how this behavior is influenced by changes in molecular structure are crucial for the initial design and development of optical devices with tailored applications and improved performance. Therefore, gaining a comprehensive understanding of the relationship between a material's structure and its properties is essential for advancing these technologies.

In this context, we have recently paved the way by investigating the mechanisms of light transmission in organic nanowires composed of 2,5-bis(arylethynyl)pyrazine-based crystals, specifically focusing on the exciton-polariton (EP) mechanism.[18] We identified key factors that influence light-guiding efficiency, such as well-ordered 1D crystal structure and short intermolecular distances along the packing direction. Furthermore, as previously proposed, the presence of internal microchannels within the crystalline structure facilitates light transmission.[19] Furthermore, it has been determined that light transmission occurs when the molecular dipole moment of the transition is perpendicular to the direction of the electric field.[20] These factors, among others, determine whether and in which direction light can be transmitted.

In the present work, we aim to take a step further on these findings by exploring another critical factor: the role of exciton binding energy as a fundamental parameter that determines the interaction strength between the electron and hole in an exciton.[21,22] The formation of an exciton is a key mechanism in light transmission within organic waveguides. Excitons, which are bound electron–hole pairs, enable the efficient transport of energy without the movement of charge carriers. Their dynamics directly influence how light propagates through the material. Properly optimized binding energy not only ensures the stability of excitons under external perturbations, such as electric fields or thermal fluctuations, but also enhances the coupling efficiency between photons and excitons.[23] This property is particularly important in organic materials, where strong exciton binding energy facilitates the formation and stability of efficient Frenkel exciton. As a result, exciton behavior is a determining factor in the performance of waveguides, affecting light confinement efficiency, directionality of light transmission and the minimization of propagation losses. Therefore, by optimizing exciton binding energy, we can design waveguides with superior photonic performance, leading to more robust and efficient optical devices.[24,25] While individual aspects of these phenomena have been explored,[20,26,27] there is a need for more comprehensive studies that connect them.

Among all the organic materials, benzothiadiazole (BTD) stands out as a versatile and extensively studied building block in different applications, including bio-imaging and fluorescence probes.[28] Its molecular structure allows straightforward chemical modification, enabling precise tuning of its HOMO–LUMO gap and photophysical properties to meet diverse application demands primarily due to its distinctive electronic and optical properties.[29–32] As a strong electron-withdrawing unit, BTD promotes efficient charge transfer in donor–acceptor systems, enhancing photoluminescence efficiency and enabling tunable optical properties. This, combined with its ability to form excellent crystalline structures, makes it an ideal candidate for effective light confinement and guiding with minimal losses. Moreover, BTD materials demonstrate exceptional thermal and photostability, essential for ensuring long-term device performance. These attributes render highly suitable for the development of optical waveguides.[33,34]

Considering the factors discussed above and building on our previous work with BTD derivatives,[33–37] the main goal of this study is to explore the optical waveguide behavior of different BTD derivatives that differ in small structural changes (Fig. 1). We aim to analyse how structural variations affect the formation of crystalline structures, as well as their influence on the key parameters governing light confinement and transmission. By gaining a more profound comprehension of these factors, we seek to improve the design of organic materials with enhanced optical waveguide properties.

Results and discussion

Synthesis

In order to conduct a study relating structure to waveguide properties, the three BTD derivatives shown in Fig. 1 have been selected. The synthetic procedure for their synthesis is summarized in Scheme 1. It can be pointed out that two of them (**B1** and **B3**) have been previously described by some authors of this article,[36,37] who have demonstrated that they crystallize in layered structures, which have shown responsiveness to external stimuli such as mechano- and thermochromism. To expand

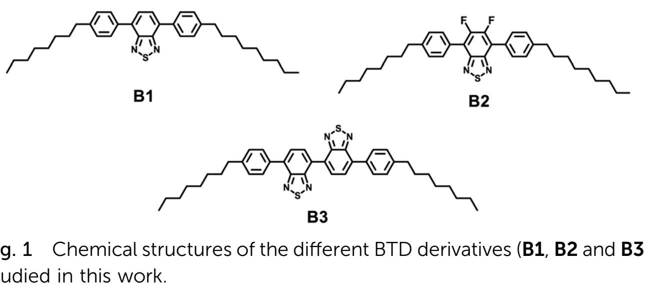

Fig. 1 Chemical structures of the different BTD derivatives (**B1**, **B2** and **B3**) studied in this work.

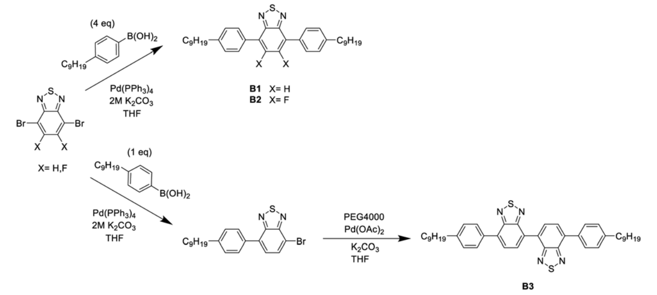

Scheme 1 Synthetic procedure of the synthesis of derivative **B1**,[36] **B2** and **B3**,[37] object of study in this work.

the crystalline diversity, in this work, a new BTD derivative (**B2**) has been synthesized by introducing two fluorine atoms into the **B1** molecule, as halogen atoms facilitate the formation of intramolecular hydrogen bonds that can influence packing and modify the crystalline structure. **B2** was synthesized through a Suzuki C–C cross coupling reaction between 4,7-dibromo-5,6-difluorobenzo[*c*][1,2,5]thiadiazole and (4-nonylphenyl)boronic acid (Scheme 1). NMR and MS spectroscopy successfully confirm the obtention of **B2**.

Self-assembling studies

The self-assembly of the BTD derivatives into crystals was carried out using the slow diffusion technique, which involves the gradual exchange of vapors between a good solvent and a poor solvent. To identify suitable solvent pairs, solubility tests were performed in various solvents to determine the good and poor ones. A solution (1 mg) of the corresponding BTD derivative in 1 mL of tetrahydrofuran or chloroform was placed in a small vial, which was then placed inside a larger vial containing 3 mL of a poor solvent, such as hexane, acetonitrile, methanol, or ethanol. The outer vial was sealed, and after 2–3 days, crystal formation was observed. The combination of good and poor solvents resulted in eight different mixtures, all of which were used for the crystallization of each compound. Among them, the THF/CH_3CN mixture was the best for obtaining crystals of **B1**, $CHCl_3$/hexane for **B2** and $CHCl_3$/MeOH for **B3**.

In order to examine the morphology of the obtained crystals, high-resolution scanning electron microscopy (HRSEM) was carried out. The images of these crystals are recorded in Fig. 2, with additional images from other solvent mixtures available in the ESI† (Fig. S3–S5).

In the case of **B1** and **B2**, well-defined rectangular crystals with excellent morphologies were obtained, characterized by sharp edges and few defects. In contrast, needle-like crystals were observed for **B3**. In all cases, the crystals exhibited promising properties for potential use as optical waveguides. The dimensions were approximately 1.5 mm in length and 400 μm in width for **B1**, 2.5 mm in length and 500 μm in width for **B2**, and 900 μm in length and 80 μm in width for **B3**.

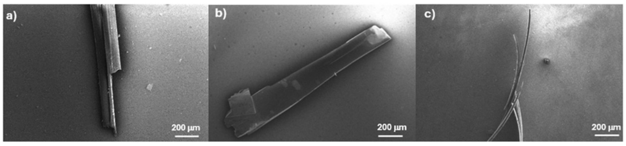

Fig. 2 HRSEM images (298 K, glass substrate) of the crystals formed by the self-assembly of (a) **B1** in THF/CH_3CN, (b) **B2** in $CHCl_3$/hexane, (c) **B3** in $CHCl_3$/MeOH.

Optical waveguiding behaviour

The optical active waveguiding behavior of crystals based on BTD derivatives, which exhibited the most favorable morphologies observed by HRSEM, was qualitatively evaluated using confocal fluorescence microscopy. For this purpose, photoluminescence (PL) microscopy images and spectra were collected for all crystals to investigate their potential optical waveguiding properties (Fig. 3). Upon photoexcitation at 355 nm, all crystals demonstrated luminescence and active optical waveguiding, efficiently transmitting light in the 450–550 nm range. More specifically, **B1** exhibited a photoluminescence spectrum with maximum at 480 nm, while **B2** showed a maximum at 459 nm, both emitting a characteristic blueish colour. The hypsochromic shift observed in the **B2** crystal compared to **B1** can be attributed to the electron-withdrawing effect of the two fluorine atoms in **B2**. On the other hand, **B3** exhibited green luminescence with a maximum at 525 nm, with a bathochromic shift relative to **B1** and **B2**. This shift is attributed to the increased conjugation induced by the combination of two BTD cores. Notably, due to their structural similarity as rectangular crystals, **B1** and **B2** exhibited 2D waveguide behavior with emission in two directions, whereas the molecular packing in **B3** resulted in a 1D waveguide behavior. Both demonstrated better optical waveguiding properties than **B3**. The factors contributing to these results will be analyzed in detail later.

Furthermore, in order to evaluate the efficiency of the optical waveguide behavior in the BTD crystals, the optical loss coefficients (OLC) were measured for all the BTDs crystals upon moving the photoexcitation (355 nm) spot along the length of the crystal while detecting the emission at one of the tips (Fig. 4). It must be pointed out that the 2D morphology of **B1** and **B2** allowed to measure OLC in two directions. The fluorescence

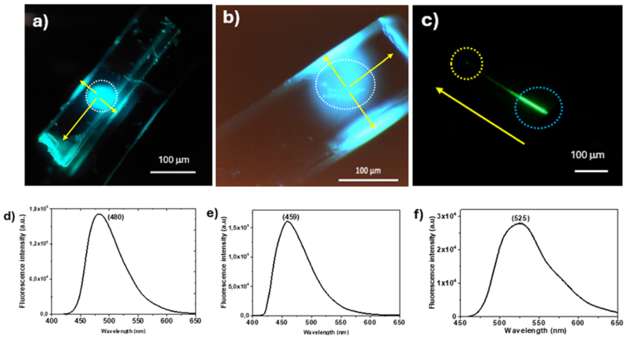

Fig. 3 PL microscopy images of (a) **B1**, (b) **B2** and (c) **B3**. PL spectra of fibers (d) **B1**, (e) **B2** and (f) **B3**. Crystals were photoexcited at 355 nm. The yellow arrows indicate the light propagation directions and blue circle indicate the excitation point and yellow circle the emission point in **B3**.

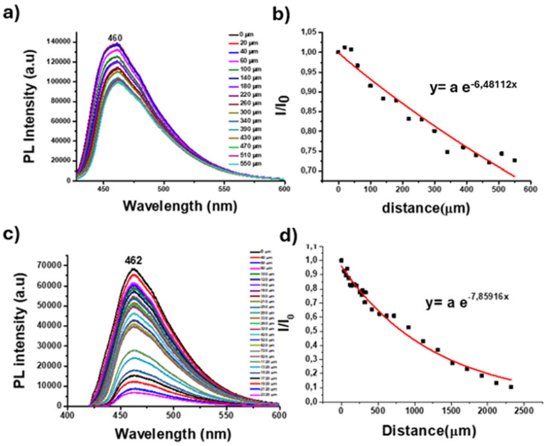

Fig. 4 (a) PL spectra of the crystals collected at the end tip upon varying the distances between the excitation and the tip of crystal of **B2** in *y* axis. (b) Ratio of the PL intensities photoexcited at the initial (I_0) and intermediate (I) positions along the *y* axis of the fiber as a function of distance (right). Red lines stand for fits to exponential laws of **B2**. Crystals were photoexcited at 365 nm. (c) PL spectra of the crystals collected at the end tip upon varying the distances between the excitation and the tip of crystal of **B2** in *x* axis. (d) Ratio between the PL intensities photoexcited at the initial (I_0) and intermediate (I) positions along the *x* axis of the fiber as a function of distance. Red lines stand for fits to exponential laws of **B2**. Crystals were photoexcited at 355 nm.

intensity (I_{out}) upon moving the pump a distance x in comparison to the initial position (I_{in}) is given by the Lambert–Beer law $I_{\text{out}} = I_{\text{in}}e^{-\alpha x}$, where I_{out} and I_{in} are the PL intensities at the output and input, respectively, x is the propagation distance and α is the absorption coefficient in μm^{-1}, which is related to the optical loss coefficient (OLC) α' (dB μm^{-1}) through the equation α' (dB μm^{-1}) $\approx 4.34\alpha$ (dB μm^{-1}) (Fig. 4 and Fig. S6, S7, ESI†). The α' values are 2.0×10^{-3} dB μm^{-1} (*y* axis) and 8.7×10^{-3} dB μm^{-1} (*x* axis) for **B1**, 2.9×10^{-3} dB μm^{-1} (*y* axis) and 3.4×10^{-3} dB μm^{-1} (*x* axis) for **B2** and 1.07×10^{-2} dB μm^{-1} for **B3** respectively, which are in the order of the best values reported in the literature.[19,38–43]

The obtained outcomes demonstrate that crystals based on **B1** and **B2** exhibit superior optical waveguide behavior in comparison to the crystal based on **B3**, with **B1** and **B2** exhibiting an OLC value that is one order of magnitude lower than that of **B3**. The excellent OLC values obtained, particularly for **B1** and **B2**, indicate the good performance of both crystals in guiding light, as the light losses along the path are very low.

Relationship between optical waveguiding and different parameters

As stated in the introduction, the main objective of this work is to establish relationships between the waveguiding property and various structural parameters, thereby deepening the understanding of light transmission mechanisms through organic structures. To achieve this, the study has been approached by considering three main aspects: (i) parameters related to the crystalline structure, including the type and mode of crystal packing, intermolecular distances, and the presence or absence of microchannels, (ii) exciton interaction energy and (iii) the relationship between the propagation direction of light and the transition dipole moment.

X-ray structure determination

Several studies have shown that the optical properties of organic crystals in the solid state are strongly influenced by molecular packing, intermolecular interactions and the external morphology of the material.[44–48] Therefore, a detailed understanding of the supramolecular organization is essential both for optimizing optical performance and for the rational design of functional materials with potential applications in optoelectronic devices. In this section, we analyze the supramolecular structure and the intermolecular interactions that give rise to the observed morphologies in the studied crystals, given their close correlation with the observed optical waveguiding behavior.

The analysis of the crystal structures by X-ray diffraction aims to assess the effect of the different modifications introduced in **B1**, **B2** and **B3** compounds on their three-dimensional packing. It should be noted that the crystal structures of the **B1** and **B3** phases have been previously reported by several of the present authors.[36,37] In this study, the previously published structural data will be used; however, the atomic labels of **B1** have been renamed in order to standardize the notation across the three structures analysed.

Compound **B1** crystallizes in the $P2_1$ space group whereas **B2** and **B3** crystallize in the $P\bar{1}$ space group. The asymmetric unit of **B1** contains two independent, non-superimposable molecules; **B2** contains one molecule per asymmetric unit; and **B3** contains five molecules, two of which are identical to each other, while the remaining three are also identical to each other but different from the first two. In all cases, the molecules have a non-planar geometry in which the benzene rings are rotated with respect to the BTD plane (Fig. S8, ESI†). This lack of planarity is more pronounced in the fluorinated derivative with dihedral angles ranging from 50.3° to 62.2° while for **B1** and **B3**, the dihedral angles range from 30.3° to 40.8°. The two BTDs in the **B3** molecule are arranged in such a way that the sulfur atoms are oriented in almost opposite directions with an angle of 141.8°.

In all three cases, the molecules associate to form dimers (Fig. 5 and Fig. S9, ESI†), with the BTD rings arranged antiparallel to minimize electronic repulsion. For **B1** and **B3**, the dimeric association occurs through π–π interactions between parallel BTDs (distances of centroids in the range of 3.66 to 3.72 Å) and CH–π interactions (distances in the range of 2.92 to 3.31 Å) between benzene rings of adjacent molecules (Table S1, ESI†). In the case of **B2**, the presence of highly electronegative fluorine atoms leads to a lateral displacement of the BTD forming dimers with only π–π interactions between two thiadiazoles with a shorter distance (3.45 Å). The different orientation of two BTD units in the **B3** molecule forms dimers in which π–π interactions can only occur between one of the two BTDs from each molecule. The second free BTD is stabilized by CH–π interactions with the benzene rings of the other molecules.

In all three structures, the dimers associate along the [100] direction mainly through non-bonding chalcogen-bonding

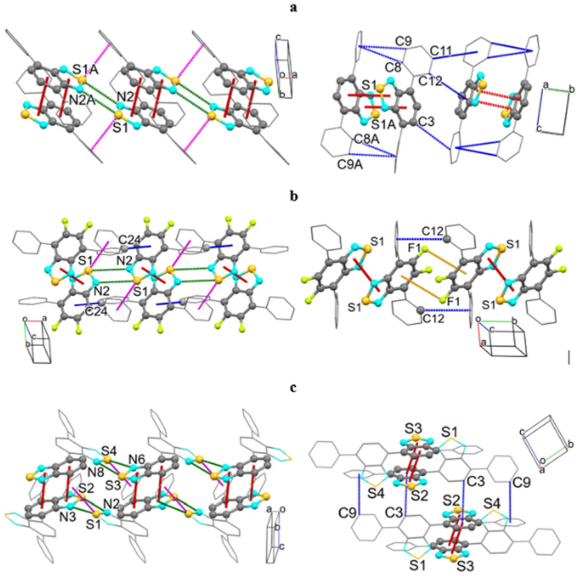

Fig. 5 Intermolecular interactions between dimers along the *a*- and *b*-axes for: (a) **B1**, (b) **B2** and (c) **B3**. The hydrogen atoms have been removed for clarity. Dashed color lines represent the different interactions as follows: red for π–π; blue for CH–π; green for S–N; orange for F–π and magenta for S–π. The parameters corresponding to these interactions are detailed in Table S1 (ESI†).

"2S–2N squares"[49] (Table S1, ESI†) with S–N distances of 3.48 Å and 3.51 Å for derivative **B1**, 3.68 Å for **B2** and 3.21–3.33 Å for **B3**. The comparatively large distance observed in derivative **B2** can be attributed to the lateral displacement of the BTD unit caused by the fluorine atoms, which likely hinders the approach of the molecules due to electronic repulsion. In contrast, the shortest distances found in **B3** are consistent with the interaction occurring exclusively through the free BTD unit, allowing more compact packing. In addition to S–N interactions, S–π interactions are also observed (Table S1, ESI†), with S-centroid distances of 3.40 Å for **B1**, 3.52 Å for **B2** and 3.83–3.93 Å for **B3**. The centroid(Bz)-*S*-centroid(BTD) angles are 115.5° for **B1** and 140.2° for **B3**. In **B2**, the sulfur atom of the BTD interacts almost frontally with the benzene ring yielding a centroid(Bz)-*S*-centroid(BTD) angle of 165.3°. In this configuration, the sp^3 lone pairs on the sulfur atom point directly at the electron cloud π of the benzene ring in an orientation unfavorable that leads to repulsive interactions.[50] The final crystal packing of **B2** is stabilized by numerous CH–π and F–π interactions, leading to a lamellar structure with layers extending in the *ab* plane (Fig. S10 and Table S1, ESI†).

Analysis of the intermolecular interactions is essential to understanding the crystal morphologies observed. In this case, the short S–N and S–π contacts suggest that these interactions play a dominant role in directing crystal growth.

Based on the intermolecular distances observed in the three derivatives, the relative strength of S–N interactions follows the order: **B3** > **B1** > **B2** and the intensity of S–π interactions varies in this other order: **B1** > **B2** > **B3**.

It is worth mentioning that short intermolecular distances (between 3.4–3.5 Å) along the packing direction result in a large overlap between adjacent π-orbitals, improving exciton–photon coupling and facilitating the light-guiding process.[26,51] This assumption, reported in the literature, could supports our results: the S–π interactions in **B1** and **B2** are of the same order as those previously reported (3.40 Å for **B1** and 3.53 Å for **B2**). In contrast, this value is 3.90 Å for **B3**. This finding could further support the superior optical waveguide behavior of **B1** and **B2** compared to **B3**.

The morphologies of the three crystals studied were simulated using the Visual Habit program of Mercury software (Fig. S11, ESI†), and the results are consistent with the experimentally observed morphologies. Fig. 3 shows that **B3** appears as one-dimensional (1D) fibers, while **B1** and **B2** form two-dimensional (2D) sheet-like structures. In all three cases, strong directional S–N interactions guide the crystal growth along the [100] direction. For **B3** these interactions dominate, leading to fiber formation with minimal interactions in other directions. In contrast, **B1** and **B2** adopt 2D structures, with **B2** being wider. **B1**, exhibit stronger S–N interactions than **B2**, which are further supported by S–π interactions along the same direction. However, in **B2**, as mentioned above, the sulfur atom's orientation relative to the benzene ring, weakens the S–π interaction, while F–π interactions promote growth along the [010] direction, resulting in wider lamellae compared to **B1**.

We have previously proposed that the emergence of microchannels in the crystals is a necessary condition for light propagation in compounds functioning as waveguides.[19] Interestingly, the crystallographic packing of **B1**, **B2** and **B3** shows the same results. To ensure that microchannels do not form due to structural defects, several crystallizations were performed under the same conditions and single-crystal X-ray diffraction measurements were taken from different batches, which consistently yielded identical unit cell parameters and packing motifs.

The crystallographic packing results in the formation of microchannels in crystals **B1** of and **B2** that extend along the [100] direction and are primarily located in the interlayer region between the alkyl chains (Fig. S12, ESI†). In contrast, although microchannels are also present in **B3**, they are significantly smaller and less abundant. For comparison, the microchannels can be approximated as rectangular, with dimensions of approximately 12.0 × 3.1 Å for **B1**, 7.8 × 2.6 Å for **B2** and 4.5 × 3.1 Å for **B3**. As shown in Fig. S12 (ESI†), the channels in **B3**, are notably reduced in both size and number compared to those in **B1** and **B2**.

These results further support the superior performance of **B1** and **B2**-based crystals as optical waveguides.

Binding energy

The transmission of light through organic crystals is possible thanks to the fulfilment of Snell's law and the exciton–polariton mechanism. An exciton is commonly defined as a quasiparticle consisting of an excited electron and the corresponding hole left behind upon its excitation. This intuitive description, originating from simplified models of electronic excitations in crystalline materials, has proven useful despite the inherent challenges of localizing particles within the quantum nanoworld where properties are best described by densities. Framing excitons in this way allows for convenient analysis using a monoelectronic, hydrogen-like model.[52] When applying this concept to molecules it is required considering the exciton as a distinct entity with its own unique electron density distribution and nuclear configuration – differing from those of the ground state.[52,53]

It is known that waveguide behavior is associated with the existence of polaritons. Polaritons are quasiparticles that result from the coupling of an exciton and a photon, enabling nonlinear effects such as waveguiding, particularly in organic molecules. These properties are enhanced when the excitons are more ''Frenkel-type'' (localized and showing a larger binding energy).[26,52,54,55]

The exciton binding energy refers to the energy required to dissociate an exciton (*i.e.*, break it apart into free charge carriers). In a previous paper[56] we demonstrate that this energy is closely tied to the value of calculated Coulomb-exchange term of excitation energies in the Hartree–Fock approach. Consequently, a dependence also exists on the calculated Coulomb – exchange term of excitation energies obtained by configuration interaction of singles (CIS) method with respect to the expected exciton binding energies.[21,22,56,57]

Therefore, we performed a CIS calculation using the CNDOL/1CS Fockian[57] method on isolated molecular structures optimized on Kohn–Sham density functional theory (KS-DFT) ωB97XD/6-31G** potential surfaces as test molecules in the ground state. The number of lowest energy mono-excited SCF determinants entering CIS was limited to four times the number of basis orbitals (4*n*) of each system in ascending order from the one of lowest eigenvalue. The CIS results of such diabatic excited state energies of **B1**, **B2**, and **B3** isolated (monomers) are presented in Table S2 (ESI†) together with experimental values of individual molecules in solution. Fig. 6 shows these results as simulated electronic state bands, using Gaussian functions with a standard deviation of 0.15 eV, considering the density of excited states (DOS-CIS) and the simulated absorption coefficient from the calculated oscillator strength. This representation also includes the Coulomb-exchange (CE) energy terms of the low-energy excited states.

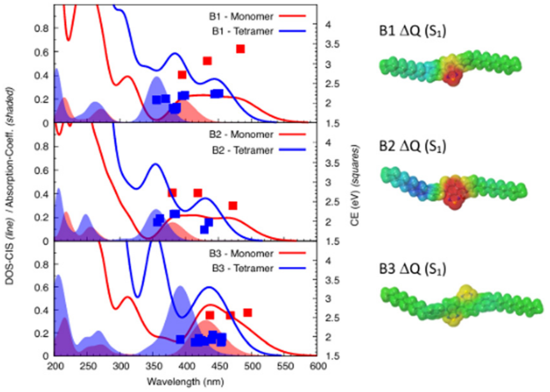

Fig. 6 Simulated density of excited states (DOS-CIS) and absorption coefficient according CNDOL/1CS calculations, including Coulomb-exchange (CE) energy terms of the low-energy excited states (left) of the monomer and tetramer crystal configurations of **B1**, **B2**, and **B3**, and calculated differentials of charge maps (right) for diabatic S_1 excitons with respect to the ground state ($\Delta Q(S_1)$) of the monomers.

The CNDOL/1CS results predict the presence of excitons corresponding to the lowest excited singlet S_1 at 480 nm (**B1**), 470 nm (**B2**) and 486 nm (**B3**). According to our results, none of them may be intensely populated by light absorption because of their very low calculated oscillator strength. However, their population could be easily reached through absorption by upper roto-vibrational modes and mostly by internal conversion from intense upper S_n's states, as the calculated models show in Fig. 6 and Table S2 (ESI†). These long wavelength S_1 states are not predicted by TD-DFT calculations, although both methods predict the allowed states in good agreement with experimental data. The reported photoluminescence maxima at 510 nm (**B1**),[36] 482 nm (**B2**) (Fig. S8, ESI†) and 511 nm (**B3**)[37] for these molecules in solution are very red shifted and thus much more congruent with the CIS|CNDOL/1CS prediction. Such S_1 excitons can enable the formation of appropriate polaritons producing the lower-energy photons to be guided in the crystal.

It must be observed that the lowest excited states appear significant and could bridge to the long wavelengths found emissions, as mentioned above. In fact, experimental absorption spectra of **B1**[36] and **B3**[37] reported evident tails of lower intensities at longer wavelength hinting the existence of such quasi-forbidden states. Furthermore, the predicted weakly absorptive nature of the S_1 state promotes waveguiding by minimizing self-absorption of the shorter wavelengths within its emission spectrum.

The calculated Coulomb-exchange (CE) energy term of S_1 states, which depends on interactions among charges upon excitations and is related to the exciton binding energy, as cited above, displays rather high values for these molecular systems. Interestingly, the first excited state of the **B1** molecule shows an exceptionally high value in this regard (see Fig. 6). This property makes it more likely that polaritons can form and function as stable wave carriers.

On the other hand, graphical representation of charge displacements upon $S_1 \leftarrow S_0$ excitations also shown in Fig. 6 indicate localization of excitons to a very Frenkel-type concentrated on the benzothiazole system on **B1** and **B2**. **B3** system shows a smaller value for CE term given the bigger size of the molecule (2.61 eV compared to 3.23 eV for **B1** and 2.75 eV for **B2**). Exciton delocalization is also significant as Fig. 6 shows. It could be a factor for disfavoring waveguiding.

To evaluate how intermolecular interactions and molecular packing affect optical properties and electronic transitions, tetramers were extracted from geometry-optimized crystal structures and analysed as representative molecular aggregates. Crystal structures were optimized at the DFT level (using the Vienna Ab Initio Simulation Package, VASP),[58] keeping experimental cell vectors fixed. Calculations employed PAW potentials, the PBE functional[59] with van der Waals corrections (BJ damping),[60] a 400 eV plane-wave cutoff, and a 3 × 3 × 1 *k*-point grid.

The lowest-energy exciton (a forbidden S_1 transition) in the tetramers exhibits a noticeable blueshift compared to the corresponding state in the **B1**, **B2**, and **B3** monomers (see Fig. 6). This trend is consistent with the experimental observation of a blueshift in the emission spectrum of the crystal relative to the molecule in solution. The shift suggests a localized, Frenkel-like exciton behavior influenced by chromophore stacking in the crystals.[51,61] The first optically allowed (bright) states also correspond to higher-energy excitons. Also note that, similarly to what was observed for the monomers, the CE values of the low-energy states of the **B1** tetramer are higher than the corresponding ones in **B2** and **B3**, which supports the hypothesis that the **B1** crystal exhibits more localized electronic excitations, or more bound excitons. These results underscore the relevance of supramolecular organization in tailoring light absorption properties in molecular materials.

Interaction between electric field and molecular transition moment

The interaction between the molecular transition dipole moment and the electric field is of crucial importance for the phenomenon of light transmission through waveguide crystals.[62] It has been demonstrated that transmission efficiency is affected by optical loss, with higher losses resulting in reduced light intensity. Optical loss can be attributed to various factors, particularly defects and inhomogeneities. In active waveguides, two main mechanisms contribute to this loss: substrate coupling (α_s), which depends on the refractive index and is direction-independent, and reabsorption (α_a), which varies with the transmission direction and the electric field's orientation relative to the molecular transition dipole moment (TDM). This can lead to anisotropic behavior: when the polarization of the incident light is nearly perpendicular to the TDM, reabsorption is minimized, thereby enhancing transmission. Conversely, parallel alignment has been demonstrated to increase reabsorption and propagation losses, thus reducing efficiency.[62]

To study this interaction, we examined the effect that polarized light would have on the absorption of the material. First, the morphology of the crystal was simulated using Visual Habit software which allowed us to identify the face with the lowest attachment energy and, therefore, the one with the largest surface area in the crystal. Assuming that this is the dominant face in the crystal, it will be the one to be in contact with the substrate and the face that will be irradiated. Secondly, we computationally determined the $S_1 \leftarrow S_0$ TDM orientation at the ωB97XD/6-31G** level. The results showed that for isolated **B1-B3** molecules extracted from the crystal structure, the orientation of the molecular TDM is parallel to the largest molecular axis (Fig. S17, ESI†). By taking into account the crystal's morphology and the arrangement of the molecules, it is possible to determine the orientation of the dipole moments with respect to the electric field.

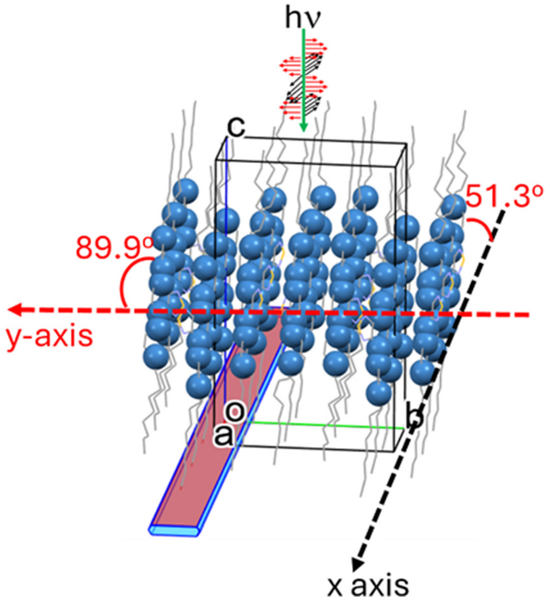

Fig. 7 Predicted morphology by Visual Habit program and orientation of molecular transition dipole moment for **B1**. The {011} face with the largest surface area is shown in red color. The molecular transition dipole moments are represented by the atoms along the long molecular axis in ball and stick style. The angle formed between the molecular transition dipole moment vector and *x*- and *y*-directions for the irradiated face is indicated. Green arrow is the incident light. Black vectors and waves indicate the longitudinal direction of polarized light relative to the red face. Red vectors and waves indicate the transversal direction of polarized light relative to the red face.

As illustrated in Fig. 7 and Fig. S18 (ESI†), it can be confirmed that, for both 2D derivatives (**B1** and **B2**), when the polarization of the incident light is oriented transversely to the irradiated {011} crystal face (along the *y*-axis), the electric field vector is nearly perpendicular to the TDM forming angles of 89.9° for **B1** and 81.9° for **B2**. This near-orthogonal arrangement leads to weaker photon–dipole coupling, resulting in reduced reabsorption and thus more efficient light transmission with lower OLC. Conversely, when the polarization of the incident light is aligned longitudinally with respect to the {011} face (along the *x*-axis), the angles between the electric field and the TDM decrease to 51.3° for **B1** and 44.8° for **B2**. This closer alignment facilitates stronger dipole–photon interactions which result in light re-absorption and slightly lower light transmission in this direction with a slightly higher OLC. These differences in TDM orientation explain the small reduction in optical loss observed along the *y*-axis. However, it is important to emphasize that the TDMs are not parallel to the polarization vector in either direction enabling light to propagate in both cases.

The **B3** crystal, despite having suitable angles for light transmission, has a fiber morphology that does not allow transmission across the transverse direction.

As a proof of concept, as it is shown in Fig. S19 (ESI†), when polarized light is used to corroborate our hypothesis, the **B1** crystal exhibits transmission in both directions, corroborating the 2D waveguide behaviour for this BTD derivative.

Conclusions

In this work, a combined experimental and theoretical study was conducted, encompassing different aspects that influence the mechanism of light transmission through organic structures. The aim is to deepen our understanding of the process and establish structure–property relationships.

For this purpose, three benzothiadiazole derivatives were chosen due to their excellent self-assembly ability. These derivatives display slight chemical structural modifications, resulting in alteration to their packing. Using the slow diffusion technique, crystals with excellent morphology and waveguide behavior have been obtained. Notably, the **B1** and **B2** crystals behave as 2D waveguides, while **B3** acts as a 1D waveguide. The variation in packing accounts for this difference. In all instances, the S–N interactions display strong directionality, steering crystal growth along the [100] direction. In the case of **B3**, fiber formation is primarily due to the dominance of S–N interactions in the [100] direction, while no notable interactions occur in other directions. The 2D waveguide behavior of the **B1** and **B2** crystals is also supported by the fact that, in both cases, the transition dipole moments of the molecules are nearly perpendicular to the electric field (close to 90° in the transversal direction and at slightly smaller angles in the longitudinal direction).

It is worth noting that the **B1** and **B2** crystals exhibit excellent 2D waveguide behavior, with optical loss values (OLC) ranging between 2 and 8.7×10^{-3} dB μm^{-1}. These values are an order of magnitude lower than those found in the case of the **B3** crystal (OLC = 1.07×10^{-2} dB μm^{-1}). A number of potential explanations have been postulated to account for this behavior. On the one hand, the disparities observed in the exciton energy calculated for individual molecules and crystals using the CIS|CNDOL/1CS Fockian method are paramount in this context. Their calculated spectra by both, this method and TD-DFT, are congruent with the first intense bands of absorption. Nevertheless, the CIS results also predict very low intensity $S_1 \leftarrow S_0$ absorptions and their corresponding lowest S_1 state energy that are congruent with the spectral appearance of the luminescence. Thus, molecules and crystals based on **B1** and **B2** exhibit more localized Frenkel excitons with higher binding energies than **B3**. This, in turn, translates into a greater ability to generate polaritons and therefore, a better capability to transmit light. On the other hand, **B1** and **B2** crystals possess a high number of microchannels in their crystalline structure, and their size is significantly greater compared to **B3** crystals.

The results obtained in this work reflect the factors that influence the mechanism of light transmission through crystalline organic structures. The knowledge derived from this work may be of great importance for the targeted and customized design of materials with improved properties as waveguides.

Experimental section

All reagents were used as purchased. Reactions with air-sensitive materials were carried out under an argon atmosphere. Microwave irradiations were performed in a Discover® (CEM) focused microwave reactor. Flash chromatography was carried out using silica gel (Merck, Kieselgel 60, 230–240 mesh or Scharlau 60, 230–240 mesh). Analytical thin layer chromatography (TLC) was performed using aluminium-coated Merck Kieselgel 60 F254 plates.

^{1}H-NMR and ^{13}C-NMR spectra were recorded on a Bruker Advance Neo NMR spectrometer operating at 500.16 MHz for ^{1}H and 125.75 MHz for ^{13}C. All spectra were performed at 298 K using partially deuterated chloroform as internal reference. Coupling constants (J) are denoted in hertz (Hz) and chemical shifts (δ) in ppm. Multiplicities are denoted as: s = singlet, d = doublet, t = triplet, m = multiplet.

UV-visible and fluorescence spectroscopy studies in solution state were conducted on a Jasco V-750 spectrophotometer and Jasco FP-8300 spectrofluorimeter, respectively. The absorption and emission spectra of **B2** were recorded in chloroform at concentration of 10^{-5} M at room temperature using standard quart cells of 1 cm width and solvents of spectroscopic grade.

HRSEM images were obtained a Zeiss Gemini SEM 500 operating at 3 kV. The corresponding crystal, obtained by slow diffusion, was deposited onto a glass substrate and the remaining solvent was slowly evaporated.

PL microscopy images were acquired with a Nikon Eclipse Ti inverted microscope with dry objectives (100× N.A. 0.8 and 20× N.A. 0.45) coupled to a Shamrock spectrometer from Andor Technology with a thermoelectrically cooled Newton EM (Andor) CCD. The excitation was obtained by appropriate filtering of the lines from a Xe lamp.

Loss coefficients in fibers were obtained upon exciting the fibers with a pulsed Nd:YAG laser (355 nm, 300 ps, 1 kHz, 30 μJ per pulse). A set of filters were employed to attenuate the photoexcitation. Detection from the fiber edge was focused in free space on to a 0.5 m length SP2558 Princeton Instruments (Acton Research) spectrometer equipped with a 600 lines per mm grating and a liquid nitrogen cooled CCD.

Theoretical calculations of the molecular geometries were carried out in the framework of density functional theory (DFT) using the hybrid B3LYP[63,64] and long-range corrected ωB97XD functional[65] in conjunction with the 6-31G** basis set.[66,67] First, we performed a preliminary conformational study to investigate all possible conformations of the three compounds in the gas phase. Next, geometry optimizations were performed without any symmetry restriction. The frequency analysis was followed to ensure that the optimized structures were stable states. Time-dependent DFT (TDDFT) calculations[68,69] (*in vacuo*) were performed to assess the excited state vertical transition energies and the molecular transition dipole moment associated to the $S_0 \rightarrow S_1$ transition. All calculations were performed with GAUSSIAN 16.[70] CIS|CNDOL/1CS calculations were performed with the NDOL8 program.[71]

Experimental data

B1 and **B3** were previously reported by some authors of this work in ref. 42 and 43.

4,7-Bis(4-nonylphenyl)-5,6-difluoro-benzo[*c*][1,2,5]thiadiazole (B2)

A mixture of 4,7-dibromo-5,6-difluoro-benzo[*c*][1,2,5]thiadiazole (100 mg, 0.30 mmol), $Pd(PPh_3)_4$ (30 mg, 0.03 mmol), and 4-nonylphenyl boronic acid (301 mg, 1.21 mmol) was prepared in 0.5 mL of 2 M aqueous K_2CO_3 and 4 mL of tetrahydrofuran (THF), then thoroughly degassed. The solution was irradiated using an Anton Paar microwave irradiator (CEM) at 130 °C (80 W) for 60 minutes. Following irradiation, the mixture was diluted with chloroform ($CHCl_3$), washed with water, and dried over magnesium sulfate ($MgSO_4$). After evaporation of the solvent, the residue was purified by chromatography using a $CHCl_3$/heptane (1 : 3) mixture, resulting in 130 mg of a white solid (compound **B2**) with a yield of 77%.

^{1}H-NMR (300 MHz, $CDCl_3$): δ 7.75 (d, 4H), 7.39 (dd, 4H), 2.70 (m, 4H), 1.68 (m, 4H), 1.45–1.27 (m, 24H), 0.89 (m, 6H). ^{13}C-NMR (300 MHz, $CDCl_3$): δ 152.2, 151.9, 150.7, 150.6, 148.8, 148.5, 144.2, 132.2, 132.1, 130.4, 128.6, 128.5, 127.6, 118.7, 118.6, 35.9, 31.9, 31.4, 29.6, 29.5, 29.4, 22.7, 14.1; FAB MS *m*/*z* 577.34 (M+).

Author contributions

Iván Torres-Moya: investigation, formal analysis, writing – review & editing. Mohammad Afsar Uddin: investigation. Sergio Gámez-Valenzuela: investigation, formal analysis, software. Javier Álvarez-Conde: investigation. Juan Cabanillas-González: investigation, formal analysis, funding. Ana L. Montero-Alejo: investigation, software, writing – review & editing, formal analysis. Ana M. Rodríguez: investigation, software, formal analysis, writing – review & editing. Luis A. Montero-Cabrera: investigation, software, formal analysis, writing – review & editing. M. Carmen Ruiz Delgado: investigation, formal analysis, writing – review & editing, funding. Berta Gómez-Lor: investigation, formal analysis, funding. Pilar Prieto: conceptualization, coordination, investigation, formal analysis, funding, writing – review & editing. The manuscript was written through contributions of all authors. All authors have given approval to the final version of the manuscript.

Conflicts of interest

There are no conflicts to declare.

Data availability

The data collected in this work has not been previously uploaded to any repository. The data that support this article have been included as part of the ESI† (added in the submission). The information has been divided in the following sections: (1) experimental details, (2) HRSEM images, (3) optical waveguiding behaviour; (4) single crystal X-ray structure; (5) binding energy; (6) TD-DFT analysis; (7) transition dipole moments analysis. CCDC 2450828 (**B2**) and 2074632 (**B3**) contains the supplementary crystallographic data for this paper. CCDC 2450829 contains the news atom labels for **B1**, which have been renamed for this paper, obtained of data previously published with CCDC 2071147.

Acknowledgements

This research was funded by the MICINN/AEI/10.13039/501100011033 and FEDER (Project PID2020-119636GB-I00, PID2022-139548NB-I00, PID2023-152323NB-I00, PID2023-150022NB-I00, PID2021-128313OB-I00), SUPRAMAT Network (RED2024-153609-T), by FEDER and Junta de Comunidades de Castilla-La Mancha (JCCM-FEDER) (Project SBPLY/21/180501/000114) and by University of Castilla-La Mancha (project 2022-GRIN-34310). J. C.-G. acknowledges the support from the Regional Government of Madrid (SYNMOLMAT), a Research Consolidation Grant (No. CNS2022-36191) and project PDC202-314587-1I00 from the Spanish Ministry of Science and Innovation, and from the "Severo Ochoa" Programme for Centres of Excellence in R&D (CEX2020-001039S/AEI/10.13039/501100011033). M. A. U. thanks to Spanish Ministry of Science, Innovation and Universities for RAMÓN Y CAJAL 2021 fellowship (Project RYC2021-034211-I) and CSIC for ATRACCIÓN DE TALENTO RAMÓN Y CAJAL 2021 (Project 20236AT033). The authors would like to thank the computer resources, technicalexpertise and assistance provided by the SCBI (Supercomputing andBioinformatics) center and the vibrational spectroscopy (EVI) lab of theResearch Central Services (SCAI) of the University of Málaga.

Notes and references

1 L. A. Coldren, S. W. Corzine and M. L. Mašanović, *Diode lasers and photonic integrated circuits*, Wiley, 2012.
2 R. Kirchain and L. Kimerling, *Nat. Photonics*, 2007, **1**, 303–305.
3 R. Chandrasekar, *Chem. Commun.*, 2022, **58**, 3415–3428.
4 W. Hourani, K. Rahimi, I. Botiz, F. P. Vinzenz Koch, G. Reiter, P. Lienerth, T. Heiser, J.-L. Bubendorff and L. Simon, *Nanoscale*, 2014, **6**, 4774.
5 B. E. A. Saleh and M. C. Teich, *Fundamentals of Photonics*, Wiley, 2019.
6 Y. Ma, Y. Zong, H. Yin, H. Lin, S. Chen and X.-D. Wang, *Adv. Opt. Mater.*, 2021, **9**, 2101481.
7 S. Chen, M.-P. Zhuo, X.-D. Wang, G.-Q. Wei and L.-S. Liao, *Photonix*, 2021, **2**, 2–24.
8 Y.-L. Shi and X.-D. Wang, *Adv. Funct. Mater.*, 2021, **31**, 2008149.
9 S. Wu, B. Zhou and D. Yan, *Adv. Opt. Mater.*, 2021, **9**, 2001768.
10 W. Ji, B. Xue, S. Bera, S. Guerin, Y. Liu, H. Yuan, Q. Li, C. Yuan, L. J. W. Shimon, Q. Ma, E. Kiely, S. A. M. Tofail, M. Si, X. Yan, Y. Cao, W. Wang, R. Yang, D. Thompson, J. Li and E. Gazit, *ACS Nano*, 2020, **14**, 10704–10715.
11 N. Mitetelo, D. Venkatakrishnarao, J. Ravi, M. Popov, E. Mamonov, T. V. Murzina and R. Chandrasekar, *Adv. Opt. Mater.*, 2019, **7**, 1801775.

12 Z. Ding, H. Shang, Y. Geng, S.-T. Zhang, Z. Huo, Z. Yang, B. Li, W. Xu and S. Jiang, *J. Phys. Chem. Lett.*, 2021, **12**, 4585–4592.

13 M. Annadhasan, S. Basak, N. Chandrasekhar and R. Chandrasekar, *Adv. Opt. Mater.*, 2020, **8**, 2000959.

14 S. Yousuf, J. Mahmoud Halabi, I. Tahir, E. Ahmed, R. Rezgui, L. Li, P. Laws, M. Daqaq and P. Naumov, *Angew. Chem., Int. Ed.*, 2023, **62**, e202217329.

15 L. Lan, L. Li, Q. Di, X. Yang, X. Liu, P. Naumov and H. Zhang, *Adv. Mater.*, 2022, **34**, 2200471.

16 J. Mahmoud Halabi, E. Ahmed, S. Sofela and P. Naumov, *Proc. Natl. Acad. Sci. U. S. A.*, 2021, **118**, e2020604118.

17 J. Li, Y. Guan, T.-T. Hao, J. Huang, Y. Chen, H. Li, P. Duan and H.-L. Xie, *Angew. Chem., Int. Ed.*, 2025, **64**, e202423395.

18 I. Chacón, J. Sánchez-Rincón, B. Gómez-Lor, M. Victoria Gomez, J. Cabanillas-González, M. C. Ruíz Delgado, I. Torres-Moya, A. M. Rodríguez and P. Prieto, *J. Mater. Chem C*, 2025, DOI: **10.1039/D5TC01067E**.

19 C. Tardío, J. Álvarez-Conde, I. Torres-Moya, A. M. Rodríguez, A. de la Hoz, J. Cabanillas-González and P. Prieto, *J. Mater. Chem. C*, 2022, **10**, 6411–6418.

20 Y. Liu, H. Hu, L. Xu, B. Qiu, J. Liang, F. Ding, K. Wang, M. Chu, W. Zhang, M. Ma, B. Chen, X. Yang and Y. S. Zhao, *Angew. Chem., Int. Ed.*, 2020, **59**, 4456–4463.

21 G. D. Scholes, *ACS Nano*, 2008, **2**, 523–537.

22 G. D. Scholes and G. Rumbles, *Nat. Mater.*, 2006, **5**, 683–696.

23 P. I. Djurovich, E. I. Mayo, S. R. Forrest and M. E. Thompson, *Org. Electron.*, 2009, **10**, 515–520.

24 S. Gambino, M. Mazzeo, A. Genco, O. Di Stefano, S. Savasta, S. Patanè, D. Ballarini, F. Mangione, G. Lerario, D. Sanvitto and G. Gigli, *ACS Photonics*, 2014, **1**, 1042–1048.

25 R. Schäfer, L. Böhner, M. Schiek, D. Hertel, K. Meerholz and K. Lindfors, *ACS Photonics*, 2024, **11**, 111–120.

26 Q. H. Cui, Q. Peng, Y. Luo, Y. Jiang, Y. Yan, C. Wei, Z. Shuai, C. Sun, J. Yao and Y. S. Zhao Cui, *et al.*, *Sci. Adv.*, 2018, **4**, eaap9861.

27 S. Kéna-Cohen and S. R. Forrest, *Nat. Photonics*, 2010, **4**, 371–375.

28 B. A. D. Neto, P. H. P. R. Carvalho and J. R. Correa, *Acc. Chem. Res.*, 2015, **48**, 1560–1569.

29 M. Echeverri, I. Martín, A. Concellón, C. Ruiz, M. S. Anselmo, E. Gutiérrez-Puebla, J. L. Serrano and B. Gómez-Lor, *ACS Omega*, 2018, **3**, 11857–11864.

30 A. Pathak, K. R. Justin Thomas, M. Singh and J.-H. Jou, *J. Org. Chem.*, 2017, **82**, 11512–11523.

31 S. Das, Y. Rout, M. Poddar, A. Z. Alsaleh, R. Misra and F. D'Souza, *Chem. – Eur. J.*, 2024, **30**, e202401959.

32 N. Méndez-Gil, S. Gámez-Valenzuela, M. Echeverri, G. H. Suyo, M. Iglesias, M. C. R. Delgado and B. Gómez-Lor, *Adv. Funct. Mater.*, 2024, **17**, 2316754.

33 R. Martín, P. Prieto, J. R. Carrillo, I. Torres, C. A. Strassert, K. Soloviova, A. M. Rodríguez, L. Sánchez and Á. Díaz-Ortiz, *Dyes Pigm.*, 2018, **151**, 327–334.

34 C. Tardío, B. Donoso, P. Fernández and I. Torres-Moya, *Chem. – Eur. J.*, 2023, 202302524.

35 A. Pinto, M. Echeverri, B. Gómez-Lor and L. Rodríguez, *Dalton Trans.*, 2022, **51**, 8340–8349.

36 M. Echeverri, C. Ruiz and B. Gómez-Lor, *CrystEngComm*, 2021, **23**, 5925–5930.

37 M. Echeverri, C. Ruiz, S. Gámez-Valenzuela, M. Alonso-Navarro, E. Gutierrez-Puebla, J. L. Serrano, M. C. Ruiz Delgado and B. Gómez-Lor, *ACS Appl. Mater. Interfaces*, 2020, **12**, 10929–10937.

38 R. Martín, A. Sánchez-Oliva, A. Benito, I. Torres-Moya, A. M. Garcia, J. Álvarez-Conde, J. Cabanillas-González, P. Prieto and B. Gómez-Lor, *J. Mater. Chem. C*, 2024, **12**, 2903–2910.

39 Y. Li, Z. Ma, A. Li, W. Xu, Y. Wang, H. Jiang, K. Wang, Y. Zhao and X. Jia, *ACS Appl. Mater. Interfaces*, 2017, **9**, 8910–8918.

40 E. Wang, J. W. Y. Lam, R. Hu, C. Zhang, Y. S. Zhao and B. Z. Tang, *J. Mater. Chem. C*, 2014, **2**, 1801–1807.

41 B. Liu, Q. Di, W. Liu, C. Wang, Y. Wang and H. Zhang, *J. Phys. Chem. Lett.*, 2019, **10**, 1437–1442.

42 H. Liu, Z. Lu, Z. Zhang, Y. Wang and H. Zhang, *Angew. Chem., Int. Ed.*, 2018, **57**, 8448–8452.

43 M. Rohullah, V. V. Pradeep, S. Singh and R. Chandrasekar, *Nat. Commun.*, 2024, **15**, 4040.

44 Y. Song, G. Pan, C. Zhang, C. Wang, B. Xu and W. Tian, *Mater. Chem. Front.*, 2023, **7**, 5104–5119.

45 D. Tian and Y. Chen, *Adv. Opt. Mater.*, 2021, **9**, 2002264.

46 P. Yu, Y. Zhen, H. Dong and W. Hu, *Chem*, 2019, **5**, 2814–2853.

47 D. K. Jones, C.-H. Cheng, Z. Li, X. Zhang, P. B. Deotare and N. Gavvalapalli, *Chem. Commun.*, 2021, **57**, 3111–3114.

48 D. Barman, M. Annadhasan, A. P. Bidkar, P. Rajamalli, D. Barman, S. S. Ghosh, R. Chandrasekar and P. K. Iyer, *Nat. Commun.*, 2023, **14**, 6648.

49 M. R. Ams, N. Trapp, A. Schwab, J. V. Milić and F. Diederich, *Chem. – Eur. J.*, 2019, **25**, 323–333.

50 R. Bhattacharyya, D. Pal and P. Chakrabarti, *Protein Eng., Design Select.*, 2005, **17**, 795–808.

51 S. Ma, S. Du, G. Pan, S. Dai, B. Xu and W. Tian, *Aggregate*, 2021, **2**, 4.

52 S. B. Anantharaman, K. Jo and D. Jariwala, *ACS Nano*, 2021, **15**, 12628–12654.

53 S. A. Mewes and A. Dreuw, *Phys. Chem. Chem. Phys.*, 2019, **21**, 2843–2856.

54 D. N. Basov, A. Asenjo-Garcia, P. J. Schuck, X. Zhu and A. Rubio, *Nanophotonics*, 2020, **10**, 549–577.

55 H. M. Gibbs, G. Khitrova and S. W. Koch, *Nat. Photonics*, 2011, **5**, 273.

56 A. L. Montero-Alejo, M. E. Fuentes, L. A. Montero and J. M. G. de la Vega, *Chem. Phys. Lett.*, 2011, **502**, 271–276.

57 L. A. Montero-Cabrera, A. L. Montero-Alejo, A. Aspuru-Guzik, J. M. García de la Vega, M. Piris, L. A. Díaz-Fernández, Y. Pérez-Badell, A. Guerra-Barroso, J. E. Alfonso-Ramos, J. Rodríguez, M. E. Fuentes and C. M. de Armas, *J. Chem. Phys.*, 2024, **160**, 214108.

58 G. Kresse and J. Furthmüller, *Phys. Rev. B: Condens. Matter Mater. Phys.*, 1996, **54**, 11169–11186.

59 J. P. Perdew, K. Burke and M. Ernzerhof, *Phys. Rev. Lett.*, 1996, **77**, 3865–3868.

60 S. Grimme, S. Ehrlich and L. Goerigk, *J. Comput. Chem.*, 2011, **32**, 1456–1465.

61 H. Li, L. Lv, K. Yuan, S. Pan and Z. Li, *Sci. Rep.*, 2023, **13**, 12357.

62 Y. Liu, H. Hu, L. Xu, B. Qiu, J. Liang, F. Ding, K. Wang, M. Chu, W. Zhang, M. Ma, B. Chen, X. Yang and Y. S. Zhao, *Angew. Chem., Int. Ed.*, 2020, **59**, 4456–4463.

63 C. Lee, W. Yang and R. G. Parr, *Phys. Rev. B*, 1988, **37**, 785–789.

64 A. Becke, *J. Chem. Phys.*, 1993, **98**, 5648–5652.

65 J.-D. Chai and M. Head-Gordon, *Phys. Chem. Chem. Phys.*, 2008, **10**, 6615–6620.

66 W. J. Hehre, R. Ditchfield and J. A. Pople, *J. Chem. Phys.*, 1972, **56**, 2257–2261.

67 M. M. Francl, W. J. Pietro, W. J. Hehre, J. Stephen Binkley, M. S. Gordon, D. J. DeFrees and J. A. Pople, *J. Chem. Phys.*, 1982, **77**, 3654–3665.

68 E. Runge and E. K. U. Gross, *Phys. Rev. Lett.*, 1984, **52**, 997–1000.

69 H. H. Heinze, A. Görling and N. Rösch, *J. Chem. Phys.*, 2000, **113**, 2088–2099.

70 M. J. Frisch, G. W. Trucks, H. B. Schlegel, G. E. Scuseria, M. A. Robb, J. R. Cheeseman, G. Scalmani, V. Barone, G. A. Petersson, H. Nakatsuji, X. Li, M. Caricato, A. V. Marenich, J. Bloino, B. G. Janesko, R. Gomperts, B. Mennucci, H. P. Hratchian, J. V. Ortiz, A. F. Izmaylov, J. L. Sonnenberg, D. Williams-Young, F. Ding, F. Lipparini, F. Egidi, J. Goings, B. Peng, A. Petrone, T. Henderson, D. Ranasinghe, V. G. Zakrzewski, J. Gao, N. Rega, G. Zheng, W. Liang, M. Hada, M. Ehara, K. Toyota, R. Fukuda, J. Hasegawa, M. Ishida, T. Nakajima, Y. Honda, O. Kitao, H. Nakai, T. Vreven, K. Throssell, J. A. Montgomery, Jr., J. E. Peralta, F. Ogliaro, M. J. Bearpark, J. J. Heyd, E. N. Brothers, K. N. Kudin, V. N. Staroverov, T. A. Keith, R. Kobayashi, J. Normand, K. Raghavachari, A. P. Rendell, J. C. Burant, S. S. Iyengar, J. Tomasi, M. Cossi, J. M. Millam, M. Klene, C. Adamo, R. Cammi, J. W. Ochterski, R. L. Martin, K. Morokuma, O. Farkas, J. B. Foresman and D. J. Fox, *Gaussian 16, Revision*, Gaussian, Inc., Wallingford CT, 2016.

71 L. A. Montero-Cabrera, A. L. Montero-Alejo, C. Bunge Molina, M. E. Fuentes, R. Crespo-Otero and N. Mora-Díez, *NDOL8*, 2023. **https://github.com/imtvi06/ndol/tree/ndol8.0.1/ndol8.0.1/Linux/raw**.